Energy & Environmental Science

Accepted Manuscript

This article can be cited before page numbers have been issued, to do this please use: S. Liu, S. Li, Q. Yang and M. Lin, *Energy Environ. Sci.*, 2025, DOI: 10.1039/D5EE01958C.

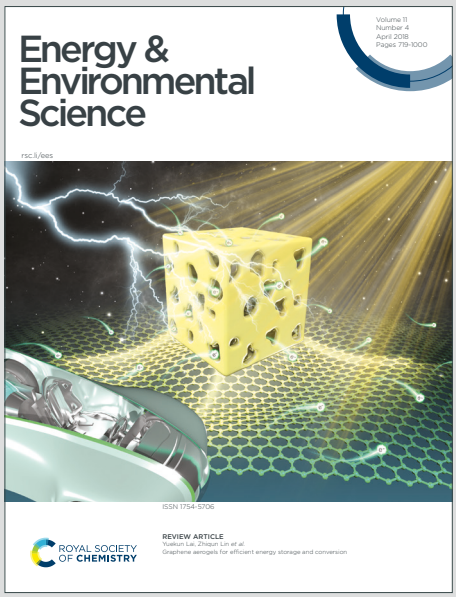

ROYAL SOCIETY OF CHEMISTRY

rsc.li/ees

View Article Online
DOI: 10.1039/D5EE01958C

Broader context

Solar interfacial evaporation has emerged as a promising and sustainable strategy to address the dual global challenges of water scarcity and increasing energy demand. Lab-scale devices have achieved high evaporation performance through advances in materials and structural design. However, scaling up from centimeter-scale units by connecting multiple modules introduces challenges, including increased system complexity, poor space utilization, and higher infrastructure costs. To enable practical, large-scale deployment, meter-scale (1 m^2) devices are increasingly viewed as the smallest effective unit for industrial applications. In this study, we present a highly efficient and scalable solar multi-stage interfacial evaporation device with an active area of 1 m^2. Our design addresses critical challenges related to material scalability, energy loss, and consistent water supply, demonstrating both high performance (3.5 L m^{-2} h^{-1}) and suitability for large-scale applications. By bridging the gap between laboratory innovation and practical implementation, this work provides a robust framework for advancing solar desalination technologies. Techno-economic analysis further indicates that reducing the cost of the photothermal absorption layer and porous membrane is essential to improving the economic viability and shortening the payback period of SMIE systems.

View Article Online
DOI: 10.1039/D5EE01958C

Scale-up of solar interfacial evaporation devices: advanced optical, thermal, and water management for efficient seawater desalination

Shang Liu[a,b,†], Shiteng Li[a,b,†], Qijun Yang[a,b], Meng Lin[a,b,*]

[a]*Department of Mechanical and Energy, Southern University of Science and Technology, Shenzhen 518055, China.*

[b]*SUSTech Energy Institute for Carbon Neutrality, Southern University of Science and Technology, Shenzhen 518055, China.*

[†]These authors contributed equally to this work.

*To whom correspondence should be addressed: linm@sustech.edu.cn

View Article Online
DOI: 10.1039/D5EE01958C

Abstract

Significant progress has been made in enhancing solar interfacial evaporation (SIE) performance at the laboratory scale, however, translating these improvements to meter-scale systems suitable for practical deployment remains limited by challenges, including material scalability, thermal losses, and non-uniform water distribution. Addressing these issues is essential for the development of modular, meter-scale evaporators as baseline units for industrial-scale desalination systems. This study presents a solar multi-stage interfacial evaporation (SMIE) device with a 1 m² active area designed to address the key limitations associated with large-scale operation systematically. The device integrates: (*i*) a scalable photothermal absorber layer based on Cu-CAT-1 metal-organic framework or carbon black, (*ii*) an inverted multi-stage configuration with optimized thermal insulation to reduce energy loss and enable latent heat recovery, and (*iii*) structured wicking channels engineered to maintain spatially uniform water transport. Under 1-sun illumination in a controlled laboratory setting, a 100 cm² prototype achieved freshwater production rates of 5.45 kg m^{-2} h^{-1} with deionized water and 3.9 kg m^{-2} h^{-1} with 3.5 wt% saline water. Outdoor testing of the full-scale 1 m² device yielded an average water production rate of 3.5 L m^{-2} h^{-1} (32 L m^{-2} day^{-1}) and an evaporation efficiency of 345%. These results confirm that the proposed SMIE design maintains high performance at increased scales and under realistic environmental conditions. A techno-economic analysis further identifies the critical role of reducing material costs, particularly the photothermal absorber and porous membrane, to enhance economic feasibility. The work provides a scalable approach to solar-driven desalination, relevant for future modular deployment in distributed and off-grid water purification applications.

Keywords: Solar thermal utilization, Solar interfacial evaporation, Heat and mass transfer, Large-scale device, Multi-stage evaporation.

View Article Online
DOI: 10.1039/D5EE01958C

Introduction

Freshwater is essential for both ecosystems and human society, and its availability is expected to become increasingly constrained in various regions due to rising demand and climate variability.[1] Solar interfacial evaporation (SIE), which leverages thermal localization, offers high evaporation efficiency [2-5] and adaptability for decentralized water purification applications.[6-10] The efficiency of devices employing thermal localization has been improved in recent developments via multi-stage designs for condensation heat recovery, [11-13] photothermal material engineering for high solar band absorption [14-16] and low thermal band emission, [17-19] and wettability tuning for a balanced evaporation and wicking rate. [20-22] With these advancements in both materials and device engineering, evaporation efficiency can be achieved in the range of 100% - 684%. [23,24]

However, most high-efficiency SIE devices are limited to lab-scale demonstrations [25,26] (typically < 100 cm²), restricting daily freshwater output to below 10 L. [27] Such capacities are insufficient to meet the basic needs of a small household (~ 3-person family), which may exceed 100 L d^{-1} when considering drinking and cooking. [28,29] Although parallel assembly of multiple centimeter-scale units can, in principle, achieve higher throughput, this approach often increases system complexity, reduces space efficiency, and adds to the overall cost of auxiliary infrastructure. To address practical water demands and reduce system complexity, a single-unit evaporator with an active area of approximately 1 m² is required. Such a unit is considered the minimal functional module for industrial-scale desalination via modular parallelization. [30]

Despite a few recent efforts to construct large-scale evaporative systems, such as a 150 m^2 array assembled from 50 individual units (unit sizes: 0.6 m × 2.0 m; 1.2 m × 1.9 m), the performance of meter-scale evaporators has generally remained low, with average freshwater production rates below 0.5 L m^{-2} h^{-1}. [30] The main limitations can be linked to: *i*) lack of uniform coating with controllable and precise mass loading, *ii*)

View Article Online
DOI: 10.1039/D5EE01958C

uncontrollable top and side convection losses, and *iii*) insufficient and non-uniform water supply for large-scale devices. Additionally, for meter-scale evaporator design, energy losses associated with the front side due to radiation and conduction from the cover to the ambient are one of the major energy losses. [31,32,33] In particular, when water needs to be collected and conventionally condensed at the cover, the heat loss, due to untamed latent heat and optical blocking by the water droplets, is one significant part that limits the efficiency of the device. [34,35]

The inverted device with a multi-stage configuration can well tackle this issue by directing the vapor downward to the condensation layer for efficient condensation, hence, to avoid otherwise optical blocking. [36-40] Meanwhile, the inverted multi-stage design offers opportunities for latent heat recovery by the evaporation layer at the next stage. However, when scaling up the design, the heat conduction losses from the edge of the device will be non-negligible due to increased height of the device. These edge losses are more pronounced at higher stage numbers due to increased edge thickness. This necessitates careful consideration of the device's thermal insulation design.

Moreover, water transport becomes more complex in larger systems. For non-swelling wicking materials, water transport follows the Lucas-Washburn capillary model, [41-43] wherein the wicking distance increases only with the square root of time. This relationship leads to a spatially heterogeneous water supply under constant solar irradiation, potentially causing local dry zones and temperature hotspots. [44] Therefore, spatially adaptive water management, through material selection or the geometric design of wicking structures, is required to match water delivery with localized evaporation demands and, hence, to prevent dry zones.

Here, we demonstrate a highly efficient and large-scale solar multi-stage interface evaporation (SMIE) device with an active area of 1 m^2 (Figure 1) that addresses the key challenges of material scalability, energy loss mitigation, and water distribution. The device incorporates: *i*) scalable photothermal layers fabricated via spray-coating of

either Cu-CAT-1 nanoparticles or carbon black, *ii*) an inverted multi-stage design with optimized edge thermal insulation to avoid optical losses due to water droplets at the cover and recycle the latent heat, and *iii*) well-designed wicking channels to mitigate the overheating problem resulting from an insufficient water supply in large-scale devices. A 10-stage prototype was constructed and evaluated under both indoor and outdoor conditions. A lab-scale device with an area of 100 cm^{-2} was developed for indoor testing. Freshwater production rates of 5.45 kg m^{-2} h^{-1} and 3.9 kg m^{-2} h^{-1} were achieved under 1-sun (1000 W m^{-2}) condition with pure water and 3.5 wt% saline water, respectively. Further, the full-scale device with an area of 1 m^2 was tested under real outdoor conditions. With an average outdoor irradiation of 651 W m^{-2}, the device collected 32 L of fresh water over 8 hours, i.e., 32 L m^{-2} d^{-1}, achieving an average water production rate of 3.5 L m^{-2} h^{-1} (efficiency of 365%) and a peak rate of 5.1 L m^{-2} h^{-1}. This 1 m^2 device can be used as a single unit to expand its application through parallel connection, to meet the different capacity needs of households or industries. This work offers practical design guidelines for the engineering of scalable passive solar evaporation devices with high performance.

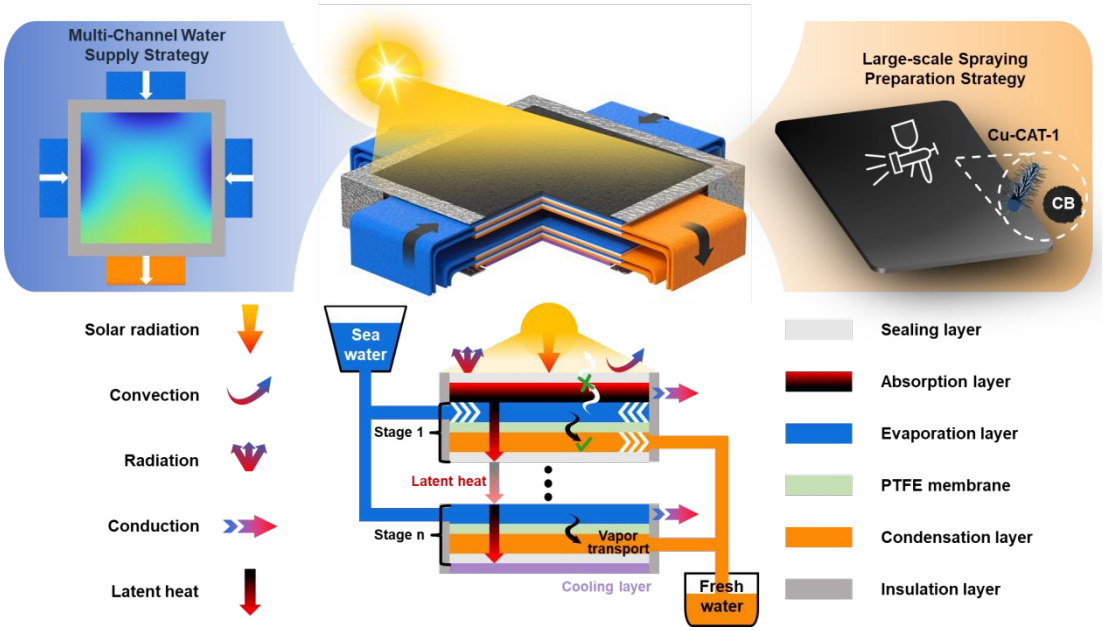

Figure 1. Schematics of large-scale solar multi-stage interface evaporation (SMIE) device. The orange box shows the spray coating strategy for scaled-up absorption layer fabrication. The blue box shows the multi-channel water supply strategy to satisfy the requirements for a high evaporation rate. The bottom part shows the schematics of SMIE device with detailed optical, heat, and mass transfer processes.

Results and discussions

Spray coating of Cu-CAT-1 MOF for meter-scale light absorber fabrication

Figure 2a and Figure 2b illustrate the scalable fabrication process of the Cu-CAT-1 MOF or CB absorption layer with high solar spectrum absorption and super-hydrophilicity for scalable solar interfacial evaporators via spray coating (Figure 2c). For Cu-CAT-1 MOF, the $Cu(OH)_2$ nanowires were used as the copper source for the synthesis of Cu-CAT-1 MOF nanorods (NRs) via hydrothermal method. Cu-CAT-1 MOF nanorods are dispersed uniformly in an anhydrous ethanol solution via ultrasonication. Subsequently, the mixed suspension solution was applied uniformly to the surface of PVA sponges, i.e., the substrate, utilizing a spray coating technique (Figure 2b). Based on the SEM pictures in Figure 2d, Cu-CAT-1 MOF NRs are well combined with polyvinyl alcohol (PVA) sponge by covering the surface of PVA fibers or filling the interspace of PVA fibers with the help of the anhydrous ethanol solution, not only preserving ultra-high light absorption performance (Figure 2f) but also exhibiting excellent water transport performance (Figure 2g).

By using the spray coating preparation methods, the size of the single piece light absorber is only limited by the size of the substrate (PVA sponge in this work). The size of the single piece of PVA sponge used in this work was 25 cm × 25 cm. For subsequent form of the target 1 m^2 device, 16 (4 × 4) pieces of PVA sponge were pieced together using assembling (Figure S1).

View Article Online
DOI: 10.1039/D5EE01958C

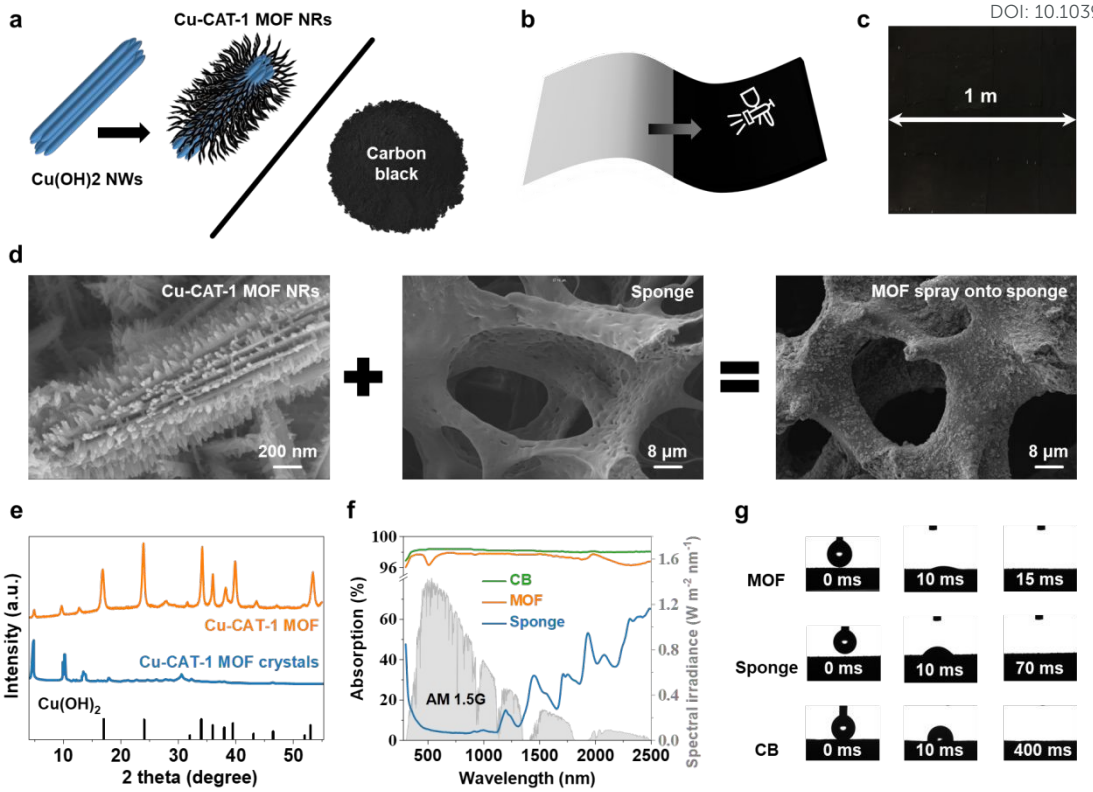

Figure 2. Large-scale spray coating strategy of Cu-CAT-1 MOF based light absorber. (a) - (c) Fabrication of a Cu-CAT-1 MOF or carbon black (CB) absorption layer through spray coating and assemble processes. (d) Scanning electron microscopy (SEM) images of the Cu-CAT-1 MOF NRs, sponge and Cu-CAT-1 MOF absorption layer. (e) XRD patterns of Cu-CAT-1 MOF、Cu-CAT-1 MOF crystals and the standard peaks for $Cu(OH)_2$ (PDF#35-0505). (f) Absorption efficiency of CB, Cu-CAT-1 MOF and PVA sponge within the typical solar wavelength range (250 nm - 2500 nm). (g) Water contact angle of Cu-CAT-1 MOF, PVA sponge and CB.

Figure 2e shows the XRD patterns of Cu-CAT-1 MOF, further confirming the successful synthesis of the target material, with peaks that closely match the Cu-CAT-1 MOF crystals with patterns form of $Cu(OH)_2$. The absorption efficiency results of CB, Cu-CAT-1 MOF, and PVA sponge in range of 250 nm to 2500 nm are shown in

Figure 2f. The average absorption efficiency of CB and Cu-CAT-1 MOF were 98.1% for CB and 97.4% with the loading concentration of 0.04 kg m^{-2}, respectively. Note that Cu-CAT-1 MOF showed inferior absorption in the band of 450 nm - 500 nm (leading to the dark blue color of material) and > 2000 nm. [45] While untreated PVA sponge shows the lowest absorption, 23.3%. The wettability of CB and Cu-CAT-1 MOF coated absorption layer are shown in Figure 2g. The wettability of PVA sponge substrate is also shown here for reference. The photographs of droplets are shown for all three cases at three different times, i.e., 0 ms, 10 ms, and time for complete absorption (15 ms for Cu-CAT-1 MOF, 70 ms for PVA sponge, and 400 ms for CB). The Cu-CAT-1 MOF shows the best performance in terms of hydrophilicity, while CB is intrinsically hydrophobic, leading to an inferior water wettability. [46] More details about the material synthesis and characterization are shown in Section S1.

Indoor test

Figure 3a shows the SMIE device with high salinity mode. The SMIE device with low salinity mode is shown in Figure S2. The two operation modes of the SMIE device are distinguished by an additional seawater outlet (the red dashed box in Figure 3a), as shown in Figure S3. The width of the additional seawater outlet is 3 cm for lab-scale SMIE device in this work as shown in Figure S17. The use of the additional seawater outlet (Figure 3a) can benefit from facile brine water discharge to avoid salt precipitation in the device at the cost of higher heat losses. [47] In this study, the low salinity mode of the device was utilized to process seawater with a salinity < 3.5 wt%. As shown in the schematic diagram of the SMIE device in Figure 1. Solar irradiation penetrated the top transparent sealing film (polyethylene, PE) and was absorbed by the absorption layer (10 cm × 10 cm) thereby heating the seawater in the evaporation layer (10 cm × 10 cm) to generate vapor. The seawater passively entered the evaporation

layer through capillary force using regenerated cellulose tissue fiber. The generated vapor was then forced to move downwards through the micropores of a PTFE membrane (12 cm × 12 cm) into the condensation layer (10 cm × 10 cm), where it condensed. The latent heat released by condensed vapor in the condensation layer was utilized to drive further distillation processes in subsequent stages. The distilled water that accumulated in the condenser was discharged into a freshwater collection tank by gravity. To maintain the bottom temperature the same as the ambient temperature, a cooling layer was incorporated at the bottom of the SMIE device to facilitate the condensation process. More details about the construction of lab-scale SMIE device are shown in Section S2.

Experiments utilized a lab-scale experimental setup under 1 sun condition produced by a AAA solar simulator, to evaluate the freshwater production performance of the SMIE device. The experimental processes for lab-scale SMIE device operating under indoor conditions in both low and high salinity modes are shown in Figure S4. The effect of the number of stages of SMIE devices with different absorption layers (CB-SMIE device - 0.04 kg m^{-2} and MOF-SMIE device - 0.04 kg m^{-2}) on evaporation rate (r_{evap}) and corresponding evaporation efficiency (η_{evap}) is shown in Figure 3b. The mass changes (m) of the collected freshwater were monitored (Figure 3c), and the average freshwater production rates for various stage designs of MOF-SMIE device, i.e., 2, 4, 6, 8, and 10 stages, were determined to be 1.74 kg m^{-2} h^{-1}, 2.88 kg m^{-2} h^{-1}, 4.15 kg m^{-2} h^{-1}, 5.10 kg m^{-2} h^{-1}, and 5.45 kg m^{-2} h^{-1}, respectively, as shown in the Figure 3b. Meanwhile, Figure 3b assesses the impact of various photothermal materials (CB - 0.04 kg m^{-2} and Cu-CAT-1 MOF - 0.04 kg m^{-2}) on the evaporation performance. We utilized a consistent preparation method to synthesize a CB absorption layer and simultaneously characterized the materials. In contrast, the r_{evap} of the CB-SMIE device is slightly lower (1.56 kg m^{-2} h^{-1}, 2.74 kg m^{-2} h^{-1}, 3.80 kg m^{-2} h^{-1}, 4.20 kg m^{-2} h^{-1} and 4.45 kg m^{-2} h^{-1}) than that of the MOF-SMIE device. This can be explained by the lower surface and

side heat losses resulting from the lower surface temperature of MOF-SMIE device (52 ^{o}C) than that of CB-SMIE device (55 ^{o}C) in wet state and n = 10 as shown in Figure 3d and Figure S5. More details about the energy breakdown of MOF-SMIE device (52 ^{o}C) and CB-SMIE device (55 ^{o}C) are shown in Figure S6. Although the surface temperature of MOF (77 ^{o}C) is higher than that of CB (75 ^{o}C) in the dry state (Figure 3d), MOF has a lower surface temperature as an absorber in SMIE device due to its superior water wettability mentioned above.

View Article Online
DOI: 10.1039/D5EE01958C

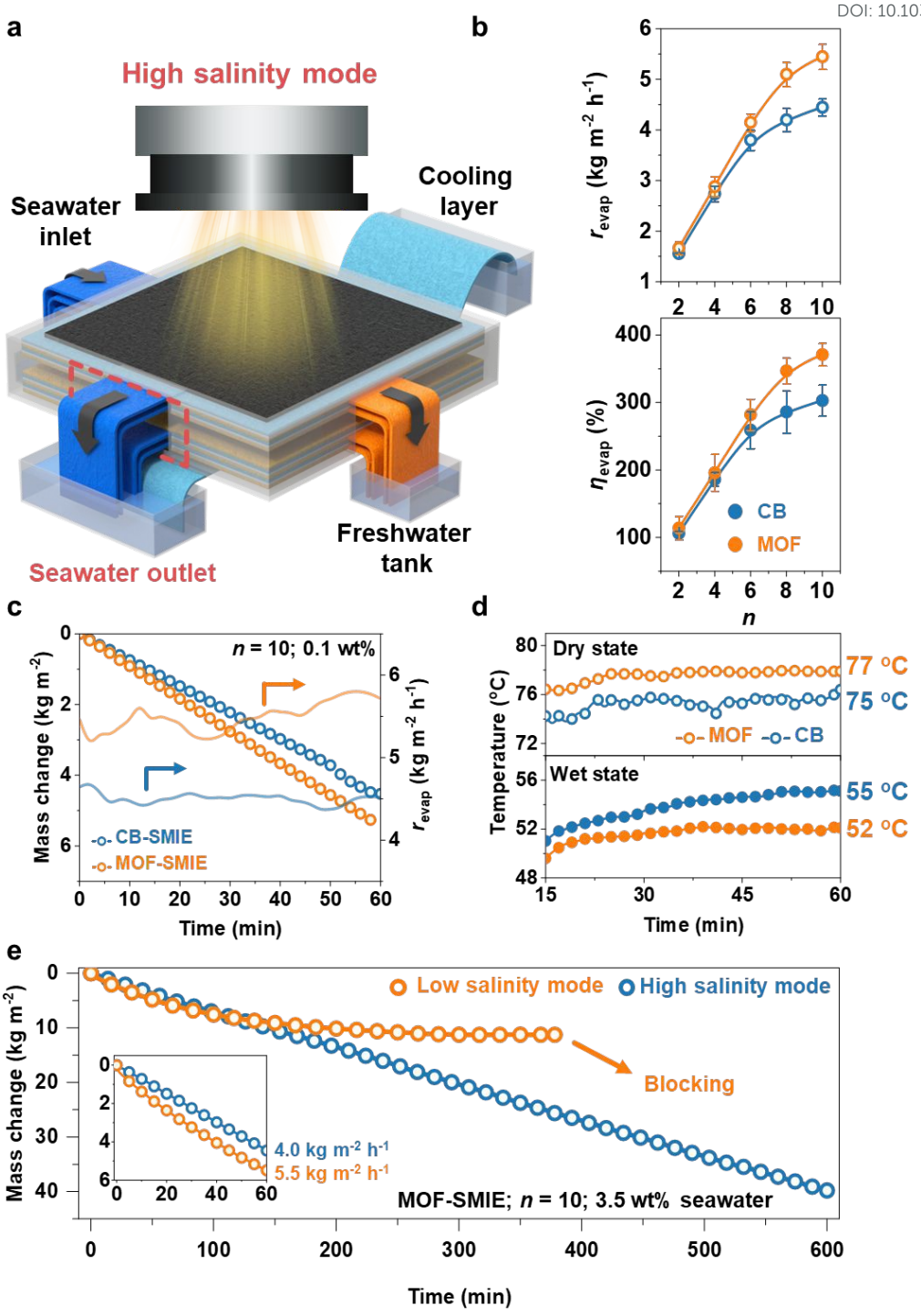

Figure 3. Laboratory test of a 100 cm² device under 1-sun condition. (a) experimental setup of the SMIE device operating in high salinity mode. (b) The evaporation rate and evaporation efficiency of CB-SMIE device and MOF-SMIE device with different stages (*n*). (c) The mass change and evaporation rate of MOF-SMIE and CB-SMIE device (*n* = 10; 0.1 wt%). (d) The surface temperatures of

CB and Cu-CAT-1 MOF absorption layer in dry and wet states. (e) The experimental comparison of the MOF-SMIE device (n = 10; 3.5 wt% seawater) in high and low salinity modes under 1 sun condition.

In addition, the effect of Cu-CAT-1 MOF loading concentration, in range of 0 kg m^{-2} - 0.08 kg m^{-2}, on the optical absorption efficiency and evaporation rate of a 2-stage SMIE was experimentally characterized as shown in Figure S7. The physical and SEM pictures of SMIE absorption layer with different Cu-CAT-1 MOF loading concentration are shown in Figure S8 and Figure S9. It can be found that the light absorption efficiency and evaporation rate increased with the increase of Cu-CAT-1 MOF loading concentration accordingly. Addition of loading did not significantly improve the evaporation rate after the loading concentration exceeded 0.04 kg m^{-2}. This is because the accumulation of Cu-CAT-1 MOF particles on the evaporator surface has a negative effect on vapor transport, although further increases in Cu-CAT-1 MOF loading concentration can improve absorption efficiency [48]. For example, the absorption efficiency and evaporation rate for SMIE device (n = 2) with MOF loading concentration of 0.04 kg m^{-2} were 92.9% and 1.75 kg m^{-2} h^{-1}, respectively. For a concentration of 0.08 kg m^{-2}, these were 97.4% and 1.79 kg m^{-2} h^{-1}, respectively. Thus, 0.04 kg m^{-2} was chosen as the optimal loading concentration for Cu-CAT-1 MOF to balance cost and efficiency in this work. Similar to the MOF, the optical and evaporation performance of the CB-SMIE device did not further increase with the increase of CB loading concentration when the loading concentration exceeds 0.04 kg m^{-2} (Figure S10).

We experimentally compared the MOF-SMIE device (n = 10) using 3.5 wt% simulated seawater under both high- and low-salinity modes at 1 sun to quantify the short-term reduction in freshwater production and to highlight the long-term stability advantages of operating in high-salinity mode. As shown in Figure 3e, the freshwater production

rate of the MOF-SMIE device (n = 10; 3.5 wt% seawater) in high salinity mode (4.0 kg m^{-2} h^{-1}) is lower than that in low salinity mode (5.5 kg m^{-2} h^{-1}) in the first 60 minutes. In low salinity mode, the freshwater production rate gradually declined and eventually stopped after approximately 200 minutes of operation, which is attributed to salt accumulation and blockage within the pores of the porous PTFE membrane due to insufficient ion discharge. In high salinity mode, although increased brine outflow resulted in greater heat loss and a reduced volume of collected condensate, the continuous removal of concentrated saltwater effectively prevented salt accumulation in the membrane, thereby enabling stable long-term operation of the SMIE device. Under 1 sun condition, i.e., 1 kW m^{-2}, the SMIE device exhibited stable operation for more than 10 hours in simulated seawater without crystallization, achieving the freshwater production rate of 3.9 kg m^{-2} h^{-1} as shown in Figure 3e. Experimental results were all obtained at a temperature of ~25 °C temperature and humidity of ~40 %.

Thermal and water management

To gain insights into the impact of device design (Figure 4a) on the water production rate of the SMIE device, a lumped parameter model was utilized for the prediction of SMIE performance and energy breakdown. More details about the model are shown in Section S3. The effect of the insulation layer's thickness ($L_{insulation}$) on evaporation rate (r_{evap}) and heat losses for the lab-scale (mm^2) SMIE device is shown in Figure 4b and Figure 4c. In general, the r_{evap} of MOF-SMIE device (n = 10) increased from 4.79 kg m^{-2} h^{-1} to 5.44 kg m^{-2} h^{-1} with increasing $L_{insulation}$ from 1 mm to 15 mm, as shown in Figure 4c. This can be attributed to the linear decrease in heat convection ($\eta_{side\text{-}conv}$; blue bar in Figure 4b) and heat conduction ($\eta_{side\text{-}cond}$; orange bar in Figure 4b) from the side of SMIE device. The radiation heat loss and convection heat loss from the absorption layer, i.e., η_{rad} and η_{conv} (red bar and green bar in Figure 4c), showed slightly

View Article Online
DOI: 10.1039/D5EE01958C

increase as a function of $L_{insulation}$, which can be associated with an increase in the top surface temperature (Figure S11). To control the $\eta_{side\text{-}cond}$ close to 5%, for the lab-scale SMIE, an insulation thickness of 5 mm is chosen (star in Figure 4b).

For the large-scale SMIE device, the active area is 1 m^2 in this study for real-world application outdoor environment. The typical wind speed in outdoor tests (v = 4 m s^{-1} in this work) is generally much higher than that of the indoor environment (v = 0.5 m s^{-1}). This will lead to an increase in η_{conv} (> 25% in all cases in Figure 4e) from top surface of SMIE. Also, the $\eta_{side\text{-}loss}$ was increased from 14.06% (Figure 4c) to 34.42% (Figure 4e) when scaling the SMIE device from 100 cm^2 to 1 m^2 at $L_{insulation}$ = 1 mm. This can be attributed to the reduction radiation loss as a result of lower top surface temperature of large-scale SMIE device compared to lab-scale SMIE device, as shown in Figure S11. For large-scale outdoor SMIE device, a minimum thickness of the insulation layer should be identified to ensure $\eta_{side\text{-}cond}$ < 5%. Hence, the minimum $L_{insulation}$ for reducing $\eta_{side\text{-}cond}$ was increased to 10 mm, as shown in Figure 4d, suggesting that the insulation layer has to be optimized under different operation conditions and device designs. The r_{evap} hence increased from 3.45 kg m^{-2} h^{-1} at $L_{insulation}$ = 1mm to 5.19 kg m^{-2} h^{-1} at $L_{insulation}$ = 10 mm for large-scale SMIE device (n = 10). The lower r_{evap} of large-scale SMIE device compared to lab-scale SMIE device is majorly due to the increased heat loss from the top surface as a result of higher wind speed as well as due to higher edge thickness as a result of multi-channel design.

Water transport management is another important aspect for optimal SMIE device designs, especially for large-scale devices where the water transport distance may exceed the wicking distance. For quantitative analysis of water transport, a finite element model was developed to describe the water transport in SMIE device for both single channel water supply (Figure 4f) and multi-channel water supply (Figure 4g). More details about the model are shown in Section S3. The numerical model was validated using experimental data, which showed a good match as long as the required

distance was > 20 cm (see Figure S12). The contour plots of local water flux at 2000 s for both cases were exhibited in Figure 4f and Figure 4g. At 0 s, the whole SMIE device was in dry condition. The dash isolines are for the water flux equal to 1.47 kg m^{-2} h^{-2} for a selected time series. 1.47 kg m^{-2} h^{-2} represents the maximum local evaporation rate without considering super thermodynamic limit phenomena in special materials, e.g., hydrogels [49,50]. Note that even at 2000 s water absorption, the area with water flux > 1.47 kg m^{-2} h^{-2}, defined as A_{wet}, was only 50%, while this area increased to ~95% for the multi-channel water supply (Figure 4h). Further, the A_{wet}/A as a function of time under various wicking channel width (L_{supply}) for both single and multi-channel designs are shown in Figure 4h. As expected, more channel numbers and larger L_{supply} are generally favorable for better water supply performance. However, for L_{supply} > 50 mm, further benefit from larger L_{supply} is minimized, indicating L_{supply} = 50 mm can be a reasonable design for a 1 m^2 SMIE device.

View Article Online
DOI: 10.1039/D5EE01958C

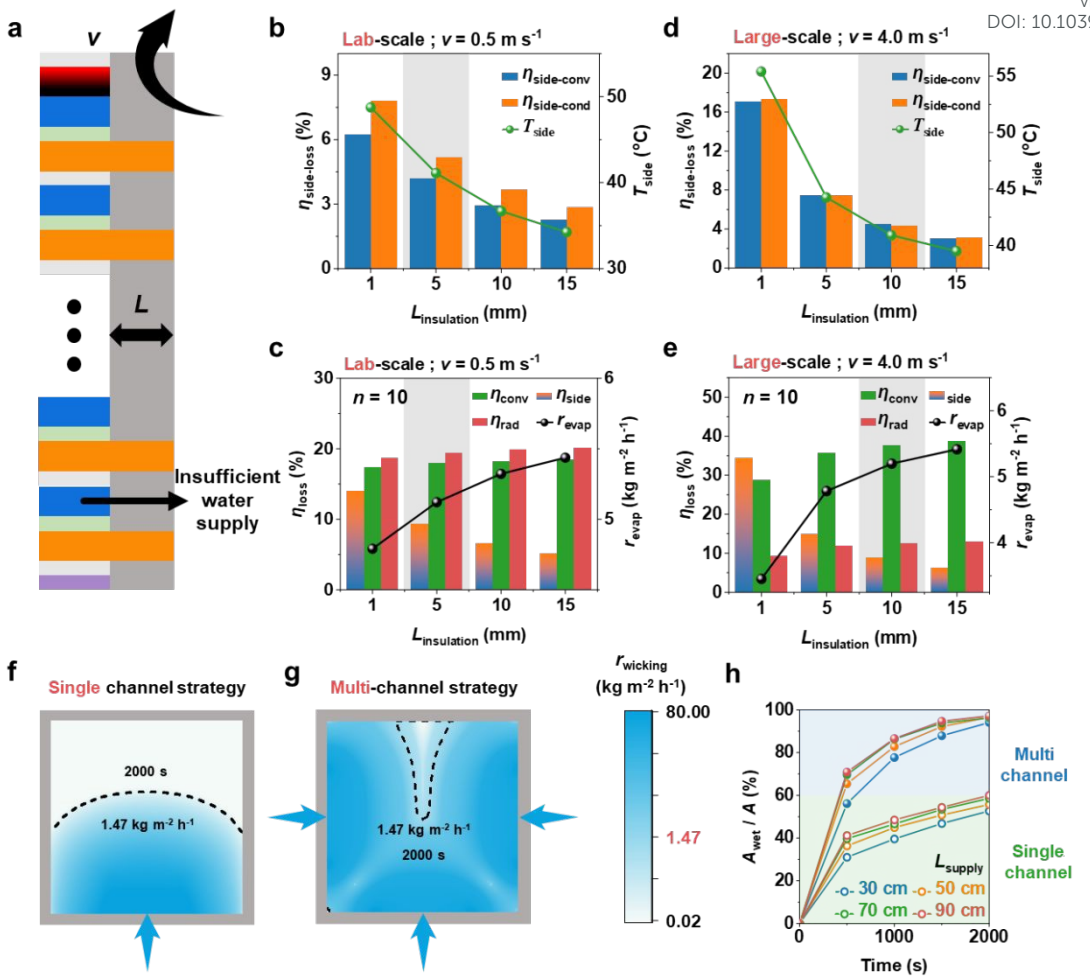

Figure 4. Impacts of heat and mass transfer on the performance of SMIE device. (a) Schematics of important parameters, the thickness of the side insulation ($L_{insulation}$) and wind speed (v) affecting the heat and mass transfer in the 1 m^2 SMIE device. The effect of $L_{insulation}$ on side (b) and overall (c) heat losses for lab-scale SMIE device (n = 10; v =0.5 m s^{-1}). The effect of $L_{insulation}$ on side (d) and overall (e) heat losses for large-scale SMIE device (n = 10; v =4.0 m s^{-1}). The diffusion distance of SMIE device with single (f) and multi-channel (g) strategy at 2000 s. (h) The wetted area with wicking rate > 1.45 kg m^{-2} h^{-1} as a function of time for both single and multiple channel strategies with different wicking channel width (L_{supply}).

View Article Online
DOI: 10.1039/D5EE01958C

Outdoor test and technoeconomic analysis

To further investigate the performance of the large-scale SMIE (1 m^2) device under real-world weather conditions, outdoor experiments were conducted on sunny days from July 25th to 27th, 2023. The detailed fabrication process of the large-scale device can be found in Figure S13 and Section S2. As shown in Figure 5a and Figure S18, the CB-SMIE device (right) and MOF-SMIE device (left) experimental setups with high salinity mode were placed adjacent to each other on the roof of SUSTech, College of engineering, North building. The width of the additional seawater outlet is 0.5 m for large-scale SMIE devices. A cooling layer was incorporated at the bottom of the SMIE device to maintain the temperature of the final layer close to the ambient temperature, facilitating the condensation process.

The outdoor experiment was carried out from 08:00 to 17:00 (local time). Figure 5b records the temperature responses of each SMIE device on July 25th, 2023. The experimental results on the 26th and 27th are shown in Figure S14. The schematic diagram of the temperature measurement point layout of the SMIE device is shown in Figure 5d. As shown in Figure 5b, the temperature of the absorption layer increased steadily in the first 3 hours, reaching ~60 ^oC for the MOF-SMIE device and 61 ^oC for the CB-SMIE device. The infrared images of CB-SMIE and MOF-SMIE devices at different times are shown in Figure S15. Although the surface temperatures of the CB-SMIE and MOF-SMIE devices were similar, the CB-SMIE device absorbed less water due to its lower water absorption capacity. Consequently, it had a lower evaporation rate and collected less condensed water compared to the MOF-SMIE device. During the 9-hour operation period, the average solar flux was measured to be 651 W m^{-2}. The water production results, presented in Figure 5b, clearly demonstrate the superior performance of the MOF-SMIE device, which produced 32 L of freshwater (32 L m^{-2} day^{-1}) with an average water production rate of 3.5 L m^{-2} h^{-1} (345% efficiency).

View Article Online
DOI: 10.1039/D5EE01958C

In addition, the accelerated aging tests were conducted. The CB-SMIE and MOF-SMIE (n = 10) devices were continuously exposed to a solar intensity of 5 suns for 24 hours. The absorption and evaporation performance of the CB-SMIE and MOF-SMIE devices before and after irradiation were then compared. As shown in Figure S16, the absorption and evaporation rates of CB-SMIE device before and after irradiation were 98.15%, 4.45 kg m^{-2} h^{-1} and 95.02%, 4.26 kg m^{-2} h^{-1}, respectively, while those of MOF-SMIE device were 97.327%, 5.45 kg m^{-2} h^{-1} and 95.88%, 5.32 kg m^{-2} h^{-1}. These results demonstrate that the evaporators are capable of maintaining high efficiency and long-term operational stability. The ion concentrations of the collected water and source water were measured by ICP-OES, and the results are shown in Figure 5c. The results demonstrate that the major ions (i.e., Na^+, Ca^{2+}, Mg^{2+}, K^+) concentrations of the collected water were all lower than 10 ppm, indicating satisfactory water quality for meeting the drinking water guideline of World Health Organization (WHO) for these ions [51]. This result demonstrates that collected clean water is safe enough for drinking.

Figure 5e compares the evaporation rate (r_{evap})/freshwater production rate (r_{fre}) and effective evaporation area of our large-scale SMIE device with state-of-the-art passive solar desalination systems reported in the literature. More details about the r_{evap} or r_{fre} and area of the works mentioned in Figure 5e are shown in Table S1. Here, the r_{evap} is represented by the solid pattern and the r_{fre} is represented by the hollow pattern. The square point in the blue area in Figure 5e represents the typical double-layer evaporator, the triangle point in the orange area represents the hydrogel evaporator, and the diamond point in the green area represents the multi-stage evaporator. Typical double-layer evaporators are more suitable for large-scale applications, and multi-stage evaporators are more conducive to enhancing the evaporation rate. Meanwhile, we think that SMIE devices in meter level have greater potential for large-scale industrial applications. Our SMIE device achieves a solar-to-vapor conversion efficiency of 365% under real outdoor conditions with an active area of 1 m^2, significantly outperforming

View Article Online
DOI: 10.1039/D5EE01958C

than most reported systems considering both performance and area simultaneously. For example, Chen et al. constructed a 150 m^2 evaporation system, achieving an average freshwater production rate of ~ 0.5 L m^{-2} h^{-1} [30]. However, the evaporation system was formed by connecting two different sizes (0.6 m × 2.0 m; 1.2 m × 1.9 m) of meter level evaporators in series, which were similar in size to our large-scale SMIE devices (1 m × 1 m) but significantly lower in evaporation performance (3.5 L m^{-2} h^{-1} in this study).

We performed a technoeconomic analysis to assess the translational potential of the SMIE device for large-scale freshwater production. Figure 5f shows the cost of freshwater production as a function of time, where the CB-SMIE (blue curve) and MOF-SMIE (orange curve) devices were compared with the bottled water price (red curve) and tap water price (green curve). The general approach of technoeconomic analysis has been demonstrated in our previous work [52]. More details about the technoeconomic analysis of SMIE can be found in Section S4. We take the time when the price of fresh water equals the price of tap water as the payback (*PP*) period. The PP as a function of evaporation rate (r_{evap}) and SMIE device cost (C_{SMIE}) is shown in Figure 5g. Although the MOF-SMIE device demonstrated better evaporation performance (point A), its higher cost ($1173.31) resulted in a significantly longer payback period (139.68 years) compared to the CB-SMIE device (point B; $122.29; 14.55 years). Furthermore, the cost proportion of the SMIE device was divided, including PTFE membrane cost, absorption layer cost, and other components cost (cellulose tissue cost, PE membrane cost and other cost), as shown in Figure 5h. When MOF was used as the photothermal material for SMIE device, the cost of absorption layer occupied a dominant position in the C_{SMIE} proportion, specifically at 94.30%. When CB was used, the proportion of the absorption layer cost in the C_{SMIE} decreased to 45.26%. The cost of porous PTFE membrane (49.09%) will dominate the C_{SMIE}. Further reducing the cost of absorption layer and porous PTFE membrane is beneficial for shortening the *PP*. For example, surface carbonized wood used as the absorption

layer exhibited lower costs, at only $ 3 per square meter [53]. Meanwhile, reducing the cost of porous PTFE membrane by half can control the C_{SMIE} to < $ 40 per square meter, with PP = 4.76 years, as shown at point C in Figure 5g and Figure 5h.

In this work, all analyses are conducted based on the operation of a single meter-scale SMIE device. Scaling up by operating multiple meter-scale devices in parallel to form a larger system still poses certain challenges. Firstly, additional costs need to be taken into account. Additional operating costs include expenses related to seawater pretreatment, costs for monitoring, collection, maintenance, labor, and electricity. According to Ref. [30], the annual operating cost is approximately $10 per year, which has a negligible impact on the payback period. The additional initial investment includes the cost of system parallelization, control systems, land leasing, and other related costs. According to Ref. [30], the control system cost accounts for the main portion of the initial investment cost, ~ $100,000, aimed at achieving high precision automation for subsequent research and insights. The overall cost can be reduced by adopting more economic control systems. Moreover, as the system's operational lifespan increases, the influence of the control system costs on the payback period gradually decreases. Meanwhile, under outdoor conditions, sunlight and warm water create favorable conditions for the growth of microorganisms, such as green algae, particularly in the freshwater collection tank. To prevent this situation, it is necessary to perform microfiltration pretreatment on seawater and regular clean and maintain the freshwater collection tank. In addition, the discharge of high-salinity brine can be harmful to the environment and should be addressed through the zero liquid discharge (ZLD) strategy.

View Article Online
DOI: 10.1039/D5EE01958C

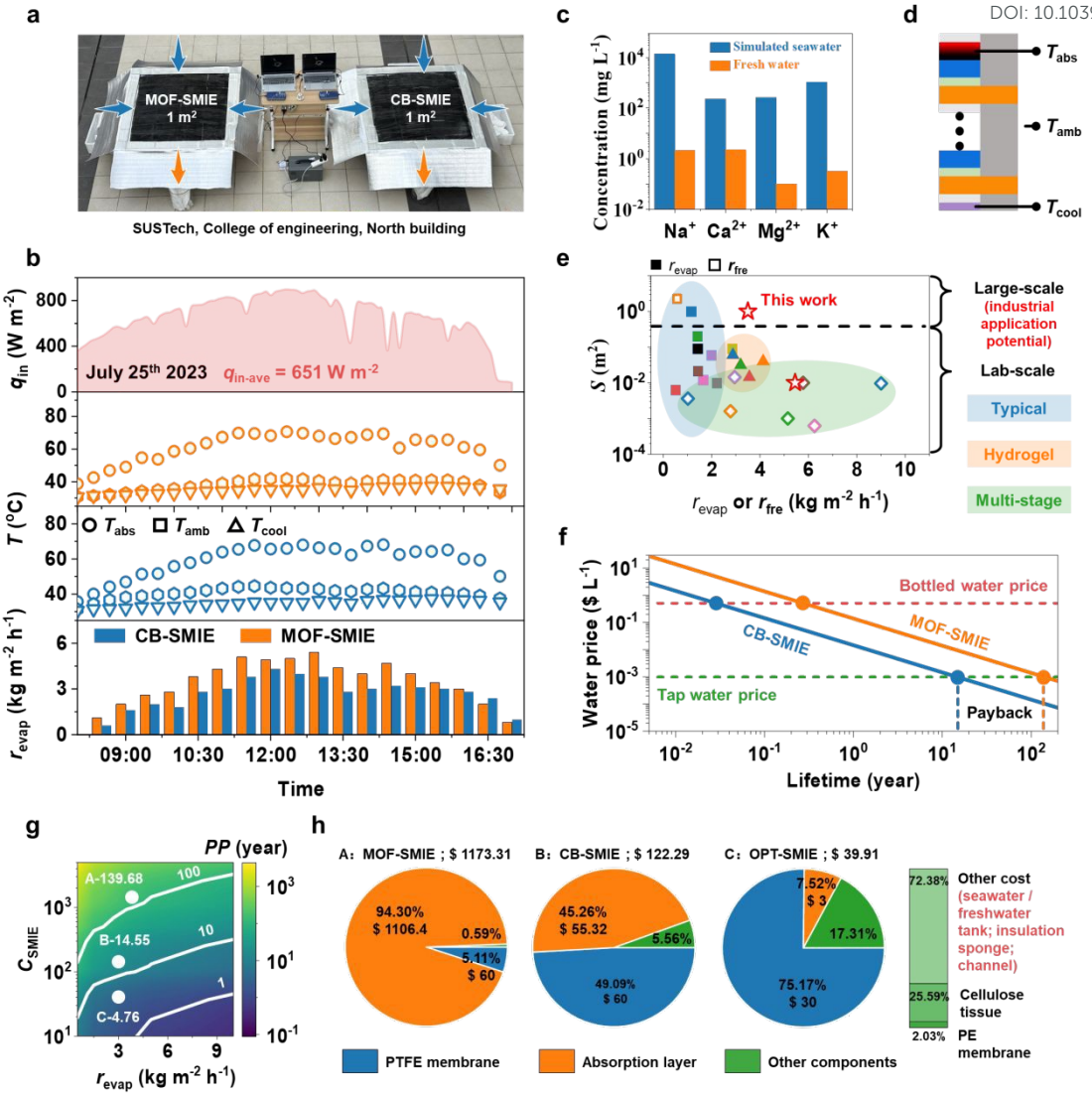

Figure 5. Outdoor tests of the large-scale SMIE device at SUSTech, college of engineering, north building on a sunny day (July 25th, 2023) and the technoeconomic analysis. (a) Experimental setup of the large-scale CB-SMIE and MOF-SMIE devices. (b) Solar radiation, temperature and water collection rate as a function of testing time. (c) The ion concentrations in raw seawater and the collected fresh water. (d) The schematic diagram of the temperature measurement point layout of the SMIE device. (e) Comparison of the evaporation rate / freshwater production rate and the area of the evaporation surface between our SMIE device and data from literature. (f) The cost of freshwater production as a function of time, where the CB-SMIE (blue curve) and MOF-SMIE (orange curve)

devices were compared with the bottled water price (red curve) and tap water price (green curve). (g) The PP as a function of evaporation rate (r_{evap}) and SMIE device cost (C_{SMIE}). (h) The cost proportion of the SMIE device, including PTFE membrane cost, absorption layer cost, and other components cost (cellulose tissue cost, PE membrane cost and other cost)

Conclusions

Our study presents a highly efficient and scalable solar multi-stage interface evaporation device with an active area of 1 m^2, designed to address the challenges of material scalability, energy losses, and insufficient water supply in large-scale solar desalination. The device integrates an inverted multi-stage configuration, a scalable photothermal absorption layer based on either Cu-CAT-1 MOF or carbon black, enhanced thermal insulation, and structured wicking channels, resulting in improved thermal performance and freshwater yield at the meter scale. The 1 m² SMIE prototype achieved a solar-to-vapor conversion efficiency of 365% under outdoor conditions, with a freshwater production rate of 3.5 L m^{-2} h^{-1}, corresponding to 32 L m^{-2} day^{-1}. These findings demonstrate that the integrated design strategies effectively enable performance scaling while maintaining efficiency, thus narrowing the gap between laboratory-scale research and field-deployable desalination technologies. Through techno-economic analysis, it is found that further reducing the costs of the absorption layer and porous membrane is key to shortening the payback period of the SMIE device. By demonstrating a scalable, high-efficiency solar interfacial evaporation system with validated performance under real-world conditions and economically relevant design parameters, this work provides a foundational framework for the development of modular, passive desalination technologies capable of addressing water scarcity in off-grid and resource-constrained environments.

View Article Online
DOI: 10.1039/D5EE01958C

Materials

N,N-dimethylformamide (DMF, 99.8%) and 2, 3, 6, 7, 10, 11-hexahydroxytriphenylene (HHTP, 95%) were purchased from Sigma-Aldrich. Copper hydroxide nanowires were purchased from Zhongke Leiming (Beijing) Technology Co., Ltd. The carbon black particles were commercially bought from Shanghai Aladdin Biochemical Technology Co., Ltd. The cellulose sponge was commercially acquired from Meilaijie Home Furnishing Flagship Store. All materials and chemicals were used as received without further purification.

Characterization

All evaporation experiments in the laboratory were conducted under a solar simulator (Newport; Sol3A). The mass change was tested by an electronic microbalance (Mettler; ME). The scanning electron microscopy (SEM) images were obtained by a FEI Nova NanoSem 450. Absorption spectra were collected using a UV-VIS-NIR spectrophotometer (Lambda 750s). More details about the experiment instruments were shown in Table S2.

Calculation of the evaporation performance

The definitions and calculation methods for evaporation rate and efficiency can be found in our previous work [48,54].

Declaration of competing interest

The authors declare that they have no known competing financial interests or personal relationships that could have appeared to influence the work reported in this paper.

Data availability

Data will be made available on request.

View Article Online
DOI: 10.1039/D5EE01958C

Acknowledgements

The authors acknowledge the National Natural Science Foundation of China under Grant No. 52376191. The Shenzhen Science and Technology Innovation Commission under Grant No. 20231120185819001, and KCXST20221021111207017, Shenzhen Key Laboratory of Intelligent Robotics and Flexible Manufacturing Systems under Grant No. ZDSYS20220527171403009, the Guangdong Basic and Applied Basic Research Foundation under Grant No. 2023A1515011595 and 2023B0303000002, and Guangdong grant under Grant No. 2021QN02L562 are also acknowledged for their support. The SEM data were obtained using equipment maintained by Southern University of Science and Technology Core Research Facilities. The computation in this work is supported by Center for Computational Science and Engineering at Southern University of Science and Technology.

View Article Online
DOI: 10.1039/D5EE01958C

References

[1] Gleick P H. Global freshwater resources: soft-path solutions for the 21st century. *Science*, 2003, 302(5650): 1524-1528.

[2] Ghasemi H, Ni G, Marconnet A M, et al. Solar steam generation by heat localization. *Nature Communications*, 2014, 5(1): 4449.

[3] Yang B, Zhang Z, Liu P, et al. Flatband λ-Ti3O5 towards extraordinary solar steam generation. *Nature*, 2023, 622(7983): 499-506.

[4] Xu N, Li J, Finnerty C, et al. Going beyond efficiency for solar evaporation. *Nature Water*, 2023, 1(6): 494-501.

[5] Xu H. Taking solar evaporation technologies to a new era. *Nature Water*, 2025: 1-2.

[6] Li H, Zhang W, Liao X, et al. Kirigami enabled reconfigurable three-dimensional evaporator arrays for dynamic solar tracking and high efficiency desalination. *Science Advances*, 2024, 10(26): eado1019.

[7] Song Y, Fang S, Xu N, et al. Solar-driven interfacial evaporation technologies for food, energy and water. *Nature Reviews Clean Technology*, 2025, 1(1): 55-74.

[8] Xu B, Ganesan M, Devi R K, et al. Hierarchically Promoted Light Harvesting and Management in Photothermal Solar Steam Generation. *Advanced Materials*, 2025, 37(5): 2406666.

[9] Mao K, Zhang Y, Tan S C. Functionalizing solar-driven steam generation towards water and energy sustainability. *Nature Water*, 2025: 1-13.

[10] Zhang L, Xu Z, Zhao L, et al. Passive, high-efficiency thermally-localized solar desalination. *Energy & Environmental Science*, 2021, 14(4): 1771-1793.

[11] Gao J, Zhang L, You J, et al. Extreme salt-resisting multistage solar distillation with thermohaline convection. *Joule*, 2023, 7(10): 2274-2290.

[12] Li X, Min X, Li J, et al. Storage and recycling of interfacial solar steam enthalpy. *Joule*, 2018, 2(11): 2477-2484.

[13] Luo X, Jiao L, Guo Y, et al. Ultrahigh freshwater production achieved by unidirectional heat transfer interfacial evaporation solar still integrated with waste heat recovery. *Energy Conversion and Management*, 2024, 304: 118226.

[14] Ren H, Tang M, Guan B, et al. Hierarchical graphene foam for efficient omnidirectional solar–thermal energy conversion. *Advanced Materials*, 2017, 29(38): 1702590.

[15] Liang H, Liao Q, Chen N, et al. Thermal efficiency of solar steam generation approaching 100% through capillary water transport. *Angewandte Chemie International Edition*, 2019, 58(52): 19041-19046.

View Article Online
DOI: 10.1039/D5EE01958C

[16] Zhang P, Li J, Lv L, et al. Vertically aligned graphene sheets membrane for highly efficient solar thermal generation of clean water. *ACS Nano*, 2017, 11(5): 5087-5093.

[17] Menon A K, Haechler I, Kaur S, et al. Enhanced solar evaporation using a photo-thermal umbrella for wastewater management. *Nature Sustainability*, 2020, 3(2): 144-151.

[18] Cooper T A, Zandavi S H, Ni G W, et al. Contactless steam generation and superheating under one sun illumination. *Nature Communications*, 2018, 9(1): 5086.

[19] Zheng S, Yu J, Xu Z. Modeling and analysis of contactless solar evaporation for scalable application. *Applied Sciences*, 2023, 13(6): 4052.

[20] Zhang Y, Xiong T, Suresh L, et al. Guaranteeing complete salt rejection by channeling saline water through fluidic photothermal structure toward synergistic zero energy clean water production and in situ energy generation. *ACS Energy Letters*, 2020, 5(11): 3397-3404.

[21] Zhang Y, Zhang H, Xiong T, et al. Manipulating unidirectional fluid transportation to drive sustainable solar water extraction and brine-drenching induced energy generation. *Energy & Environmental Science*, 2020, 13(12): 4891-4902.

[22] Shao Y, Shen A, Li N, et al. Marangoni effect drives salt crystallization away from the distillation zone for large-scale continuous solar passive desalination. *ACS Applied Materials & Interfaces*, 2022, 14(26): 30324-30331.

[23] Xu Z, Zhang L, Zhao L, et al. Ultrahigh-efficiency desalination via a thermally-localized multistage solar still. *Energy & Environmental Science*, 2020, 13(3): 830-839.

[24] Zhang L, Xu Z, Bhatia B, et al. Modeling and performance analysis of high-efficiency thermally-localized multistage solar stills. *Applied Energy*, 2020, 266: 114864.

[25] Wang Y, Wei T, Wang Y, et al. Quasi-waffle solar distiller for durable desalination of seawater. *Science Advances*, 2024, 10(22): eadk1113.

[26] Wang Y, Zhao W, Lee Y, et al. Thermo-adaptive interfacial solar evaporation enhanced by dynamic water gating. *Nature Communications*, 2024, 15(1): 6157.

[27] Liu S, Huang C, Huang Q, et al. A new carbon-black/cellulose-sponge system with water supplied by injection for enhancing solar vapor generation. *Journal of Materials Chemistry A*, 2019, 7(30): 17954-17965.

[28] Fan L, Liu G, Wang F, et al. Domestic water consumption under intermittent and continuous modes of water supply. *Water Resources Management*, 2014, 28: 853-865.

[29] Xu N, Zhang H, Lin Z, et al. A scalable fish-school inspired self-assembled particle system for solar-powered water-solute separation. *National Science Review*, 2021, 8(10): nwab065.

[30] Chen Y, Shen L, Qi Z, et al. Large-scale implementation of solar interfacial desalination. *Nature Sustainability*, 2025, 8(2): 162-169.

View Article Online
DOI: 10.1039/D5EE01958C

[31] Luo X, Shi J, Zhao C, et al. The energy efficiency of interfacial solar desalination. *Applied Energy*, 2021, 302: 117581.

[32] Zheng S, Oelckers B, Khandelwal A, et al. Interfacial solar evaporation for sustainable brine mining. *Nature Water*, 2025: 1-3.

[33] Pu Y, Lin W, Yao X, et al. Large-scale 3D printed fouling-resistant self-floating evaporator. *Nature communications*, 2025, 16(1): 3677.

[34] Liu S, Huang C. A stable and flexible carbon black/polyethyleneimine‐bacterial cellulose photothermal membrane for high‐efficiency solar vapor generation. *International Journal of Energy Research*, 2020, 44(11): 8904-8918.

[35] Li X, Ni G, Cooper T, et al. Measuring conversion efficiency of solar vapor generation. *Joule*, 2019, 3(8): 1798-1803.

[36] Kim H T, Philip L, McDonagh A, et al. Recent advances in high-rate solar-driven interfacial evaporation. *Advanced Science*, 2024, 11(26): 2401322.

[37] Chen Y, Luo X, Gu X, et al. The energy efficiency of multistage interfacial desalination: Comprehensive analysis and further improvement strategy. *Desalination*, 2023, 568: 117000.

[38] Liu S, Li S, Yang Q, et al. Synergistic optical and thermal management for solar water and electricity co-generation via a front-side coupling strategy. *Cell Reports Physical Science*, 2025.

[39] Nawaz F, Yang Y, Zhao Q, et al. Can the interfacial solar vapor generation performance be really “beyond” theoretical limit? *Advanced Energy Materials*, 2024, 14(22): 2400135.

[40] Zhao Q, Wei Y, Yang Y, et al. Architectural and real-time monitoring design of multi-stage solar still for solar water purification. *Renewable Energy*, 2025: 122660.

[41] Cai J, Jin T, Kou J, et al. Lucas–Washburn equation-based modeling of capillary-driven flow in porous systems. *Langmuir*, 2021, 37(5): 1623-1636.

[42] Hamraoui A, Nylander T. Analytical approach for the Lucas–Washburn equation. *Journal of Colloid and Interface Science*, 2002, 250(2): 415-421.

[43] Dimitrov D I, Milchev A, Binder K. Capillary rise in nanopores: molecular dynamics evidence for the Lucas-Washburn equation. *Physical Review Letters*, 2007, 99(5): 054501.

[44] Hou L, Li S, Qi Y, et al. Advancing Efficiency in Solar-Driven Interfacial Evaporation: Strategies and Applications. *ACS Nano*, 2025.

[45] Ma Q, Yin P, Zhao M, et al. MOF-based hierarchical structures for solar-thermal clean water production. *Advanced Materials*, 2019, 31(17): 1808249.

[46] Asthana A, Maitra T, Büchel R, et al. Multifunctional superhydrophobic polymer/carbon nanocomposites: graphene, carbon nanotubes, or carbon black?. *ACS Applied Materials & Interfaces*, 2014, 6(11): 8859-8867.

View Article Online
DOI: 10.1039/D5EE01958C

[47] Liu S, Li S, Lin M. Understanding interfacial properties for enhanced solar evaporation devices: from geometrical to physical interfaces. *ACS Energy Letters*, 2023, 8(4): 1680-1687.

[48] Liu S, Huang C, Luo X, et al. High-performance solar steam generation of a paper-based carbon particle system. *Applied Thermal Engineering*, 2018, 142: 566-572.

[49] Zhou J, Gu Y, Liu P, et al. Development and evolution of the system structure for highly efficient solar steam generation from zero to three dimensions. *Advanced Functional Materials*, 2019, 29(50): 1903255.

[50] Zhao F, Zhou X, Shi Y, et al. Highly efficient solar vapour generation via hierarchically nanostructured gels. *Nature Nanotechnology*, 2018, 13(6): 489-495.

[51] Frisbie S H, Mitchell E J, Dustin H, et al. World Health Organization discontinues its drinking-water guideline for manganese. *Environmental Health Perspectives*, 2012, 120(6): 775-778.

[52] Liu S, Yang Q, Li S, et al. A comprehensive review of salt rejection and mitigation strategies in solar interfacial evaporation systems. *Desalination*, 2024: 118507.

[53] Li T, Liu H, Zhao X, et al. Scalable and highly efficient mesoporous wood-based solar steam generation device: localized heat, rapid water transport. *Advanced Functional Materials*, 2018, 28(16): 1707134.

[54] Liu S, Huang C, Luo X, et al. Performance optimization of bi-layer solar steam generation system through tuning porosity of bottom layer. *Applied Energy*, 2019, 239: 504-513.

View Article Online
DOI: 10.1039/D5EE01958C

Data availability

Data will be made available on request.